# Simulator of Non-homogenous Alumina and Current Distribution in an Aluminum Electrolysis Cell to Predict Low-Voltage Anode Effects

LUKAS DION, LÁSZLÓ I. KISS, SÁNDOR PONCSÁK, and CHARLES-LUC LAGACÉ

Perfluorocarbons are important contributors to aluminum production greenhouse gas inventories. Tetrafluoromethane and hexafluoroethane are produced in the electrolysis process when a harmful event called anode effect occurs in the cell. This incident is strongly related to the lack of alumina and the current distribution in the cell and can be classified into two categories: high-voltage and low-voltage anode effects. The latter is hard to detect during the normal electrolysis process and, therefore, new tools are necessary to predict this event and minimize its occurrence. This paper discusses a new approach to model the alumina distribution behavior in an electrolysis cell by dividing the electrolytic bath into non-homogenous concentration zones using discrete elements. The different mechanisms related to the alumina distribution are discussed in detail. Moreover, with a detailed electrical model, it is possible to calculate the current distribution among the different anodic assemblies. With this information, the model can evaluate if low-voltage emissions are likely to be present under the simulated conditions. Using the simulator will help the understanding of the role of the alumina distribution which, in turn, will improve the cell energy consumption and stability while reducing the occurrence of high- and low-voltage anode effects.

https://doi.org/10.1007/s11663-018-1174-2


## I. INTRODUCTION

PRIMARY aluminum production contributes significantly to greenhouses gases (GHG) emissions due to the production of carbon dioxide ($CO_2$), inherent to the chemical reactions occurring in the electrolysis cells using carbon anodes. However, the aluminum industry is also known as one of the two most important anthropogenic emitters of perfluorocarbons (PFC) along with the semiconductor industry. These types of gas, namely the tetrafluoromethane ($CF_4$) and the hexafluoroethane ($C_2F_6$), are known to be produced when the cell's current distribution diverges from the normal operating range due to the lack of alumina in the electrolyte, thus leading to a harmful event called anode effect.

In the 1990s, many researchers[1–4] demonstrated that a relationship exists between the polarized anode effect duration and the amount of PFC gas generated during the occurrence of the anode effect. However, such relation is consistent with a specific type of anode effects which perturbs strongly the cell behavior by significantly increasing the global cell voltage above the normal operation level, thus generating important amounts of heat while increasing the level of cell instability. Since the cell voltage is a well-followed indicator, such events can be easily detected by the cell control system and are classified as high-voltage anode effect (HVAE). However, recent studies (early 2010s)[5–10] demonstrated that PFC emissions can also be generated locally by similar mechanisms under only a few number of anodes. Redistribution of the current might prevent propagation of this phenomenon and only a local increase in resistance is observed with no significant increase in the global cell voltage.[11] Depending on the cell technologies, the annual emissions resulting from low-voltage anode effects (LVAE) can be even more important that the emission level resulting from HVAE.[12]

Even though LVAE detection is very difficult currently in a fully operating smelter, some key indicators presented in the literature can be used in order to create a simulation tool which could help to improve the electrolysis process while reducing the risk of LVAE. To achieve this goal, a simulator could provide information about the evolution of non-homogeneity of the alumina

LUKAS DION, LÁSZLÓ I. KISS, SÁNDOR PONCSÁK are with the GRIPS, Université du Québec à Chicoutimi, 555 boul. de l'Université, Chicoutimi, QC G7H 2B1, Canada. Contact e-mail: lukas.dion@uqac.ca CHARLES-LUC LAGACÉ is with the Aluminerie Alouette Inc., 400 Chemin de la Pointe-Noire, C.P. 1650, Sept-Îles, QC G4R 5M9, Canada.

Manuscript submitted September 8, 2017.
Article published online January 29, 2018.

distribution inside the electrolytic bath as well as information regarding non-uniform current distribution among the anodes.

In this article, the different mathematical sub-models used in the development of this simulator are presented and discussed, focusing on alumina feeding, alumina dissolution, the diffusive and convective transport within the electrolytic bath, alumina consumption by electrolysis, the cell electrical model, and LVAE risk assessment. This simulator was validated by comparing the data to four specific experimental scenarios tested at Aluminerie Alouette. Finally, possible improvements of the process resulting from using this simulator are presented and discussed.

## II. GENERATION OF PFC DURING HIGH-VOLTAGE AND LOW-VOLTAGE ANODE EFFECTS

Anode effects occur in a cell when an insufficient amount of dissolved alumina is present in the bath. When this condition happens, the passage of the electrical current cannot be sustained longer by the normal electrolysis reaction (Eq. [1]). Therefore, there is an increase in the anodic overvoltage, leading to the occurrence of secondary reactions within the electrolytic bath (Eqs. [2] to [4], where $E^0$ is the decomposition potential).

$$2Al_2O_{3(diss)} + 3C_{(s)} \rightarrow 4Al_{(l)} + 3CO_{2(g)} \quad E^0 = -1.18V \quad [1]$$

$$2AlF_{3(diss)} + Al_2O_{3(diss)} + 3C_{(s)} \rightarrow 4Al_{(l)} + 3COF_{2(g)} \quad E^0 = -1.88V \quad [2]$$

$$4Na_3AlF_{6(l)} + 3C_{(s)} \rightarrow 4Al_{(l)} + 3CF_{4(g)} + 12NaF_{(diss)} \quad E^0 = -2.58V \quad [3]$$

$$2Na_3AlF_{6(l)} + 2C_{(s)} \rightarrow 2Al_{(l)} + C_2F_{6(g)} + 6NaF_{(diss)} \quad E^0 = -2.80V. \quad [4]$$

As the anodic overvoltage increases, different reactions will be triggered in the cell. Reactions [3] and [4] are commonly known to be the main reactions generating PFC during HVAE because the cell voltage increases significantly (> 10 volts) and the fluoride-based bath electrolyzes itself in order to maintain the rate of passage of the current. On the other hand, Reaction [2] is plausibly the main reaction leading to PFC generation during LVAE as the increase in anodic overvoltage is not occurring globally in the cell but rather locally under only a small number of anodes where the local conditions changed due to a low alumina concentration. However, $COF_2$ is thermodynamically unstable under the electrolysis bath conditions and will rapidly decompose to form $CF_4$ or $C_2F_6$ following Reactions [5] and [6], where $K$ is the kinetic of the reactions.

$$2COF_{2(g)} + C_{(s)} \rightarrow 2CO_{(g)} + CF_{4(g)} \quad K = 94.8 \quad [5]$$

$$3COF_{2(g)} + 2C_{(s)} \rightarrow 3CO_{(g)} + C_2F_{6(g)} \quad K = 1.2 \times 10^{-3}. \quad [6]$$

Several qualitative investigations were performed to determine which events or elements of the cell behavior can lead to LVAE. In agreement with the theoretical assumptions, a low alumina concentration was found to be one of the most important elements that can lead to LVAE.[8,9,11,13–17] However, most of these studies also demonstrated that the current density and the anodic overvoltage were strongly related to LVAE as well[8,9,11,13,15,16] due to the interdependence of all these elements. Coherently with these results, the onset of LVAE often appears a short while after an anode change[8,9,12,16,17] which indicates that the perturbation of the current distribution plays an important role in this phenomenon.

Only a few studies resulted in a quantitative relationship to account for the amount of PFC emitted during LVAE. Using experimental data, Chen *et al.*[13] demonstrated that an exponential increase of the PFC emitted can be expected when the alumina concentration in the bath is below 2 pct wt and more evidently below 1.5 pct wt. However, as the alumina concentration is rarely measured during normal operation of an electrolysis cell, such a model can hardly be used to quantify PFC emissions resulting from LVAE. To counter this problem, the authors of this article previously developed a complex multivariate model[18] that uses seven, monitored cell indicators to account for the level of PFC emitted during LVAE. The results of this analysis demonstrated that the dominant cell indicator that can reveal information on the presence of LVAE in the electrolysis cell is the standard deviation among all individual anode currents.

## III. DEVELOPMENT OF THE SIMULATOR

In order to study or even predict the onset of LVAE, the electrolysis cell cannot be treated as a homogenous entity, and the spatial distribution of the intensive parameters like alumina concentration, electric potential, *etc.*, must be analyzed to correctly assess the impact of changes in its local behavior. Complex CFD-based continuum models[19–21] are regularly used to describe the temporal and spatial variations in the alumina concentration of the electrolytic bath. However, such models require a significant computing time and the details and precision exceed the level required for the LVAE study. For this reason, a new methodology is proposed that represents the electrolytic bath as a non-homogenous body with only twenty discrete volumes. Each of these volumes is considered as a lumped

system representing the individual anodic assemblies (2 anodes per yoke) with their own specific alumina concentration. In parallel, the overall cell current is divided non-uniformly and distributed among these volumes according to the solution of an electrical model that permits to simulate the respective change in current distribution caused by various elements. Under industrial conditions, the twenty volumes may be different due to different ledge profile across the periphery of the cell. However, in the simulator, the total mass of electrolyte within each distinct volume is considered to be the same.

The mathematical model is based on the balance equations of the mass of alumina and that of the electric charge with respect to the estimated current efficiency of the cell. Hence, the alumina depletion rate is coupled with the current from each zone to adequately represent the correlation between concentration and current distribution. We did not perform the thermal energy and momentum balance calculations inside our model. Obviously, the bath movement has a very important effect on the alumina distribution so we used external literature data for imposing an estimated and simplified velocity field. Also for the sake of simplifying the calculations, we assumed a constant average temperature in the bath. Finally, the homogeneity of the predicted individual anode current distribution is also evaluated to predict LVAE emissions.

For each time step, different mathematical models are used sequentially to evaluate the transient variation in the alumina concentration, the current distribution, and the risk of LVAE emissions. The seven different modules of the overall model are illustrated in Figure 1 and they will be thoroughly discussed in the following sections of this paper. The algorithm and the solver for the simulator and its modules were completely developed and coded by the authors using Matlab® R2016b (student license).

## IV. INPUT DATA, INITIAL CONDITIONS

In order to run the simulator and all its modules, initial information such as the cell amperage, the expected current efficiency, the total mass of electrolyte in the cell, and its composition (excess $AlF_3$ and $CaF_2$ concentrations) are necessary. Additionally, the initial alumina distribution in the cell is required as an initial condition. This distribution is either prescribed according to the scenario that we want to study, or it is based on experimental data.

The mathematical model is based on an explicit method, advancing in time, and hence data are extrapolated based on the set of data in the previous time step. As it is well known for such numerical schemes, the time step needs to be adequately chosen to assure the numerical stability of the solution. Equation [7] was used to evaluate the time step's maximum value in order to respect numerical stability during two-dimensional diffusion mass transfer. To assure a consistency between the numerical results and the phenomenon simulated, the time step ($\Delta t$) (seconds) has to be smaller than the ratio between the squared distance that separates the volumes considered ($(\Delta x)^2$) ($m^2$) and the equivalent diffusion coefficient ($D_{eq}$) ($m^2/s$) (presented later in this paper) multiplied by a ratio ($n$) (–) depending on the dimension of the problem. In this case, n is equal to 4 as the study is two-dimensional.

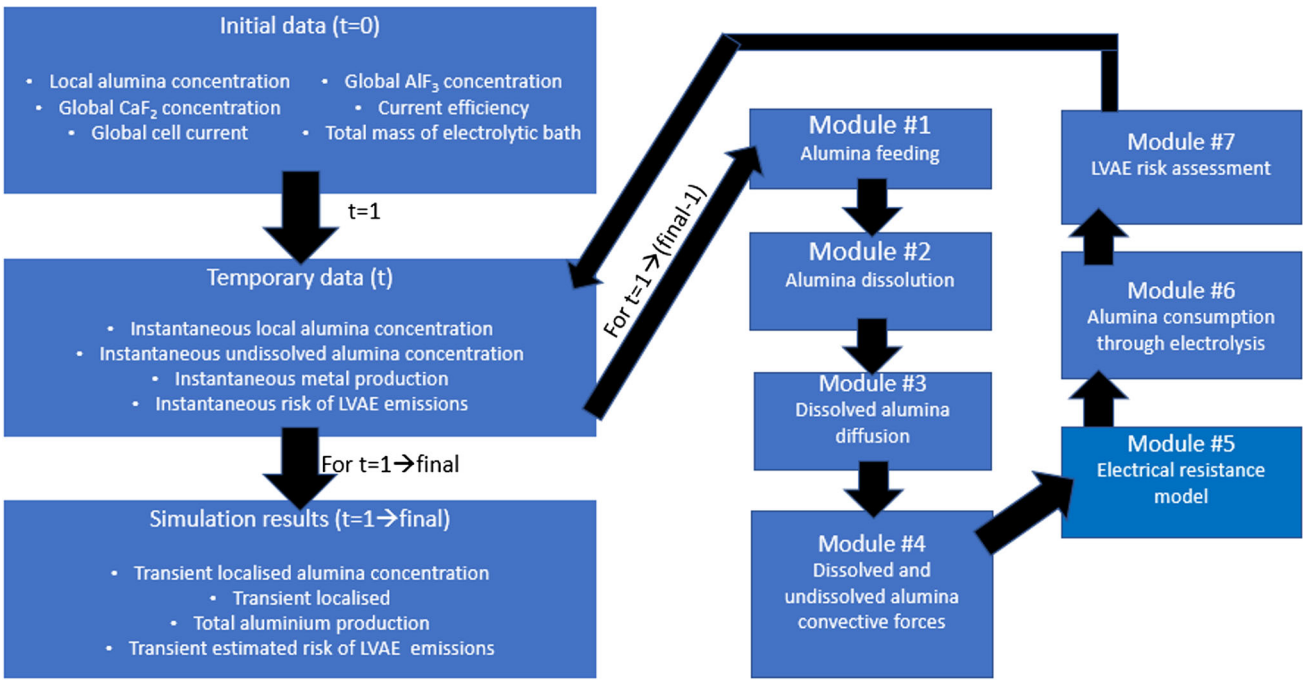


Fig. 1—Sequential structure of the algorithms used in the simulator.

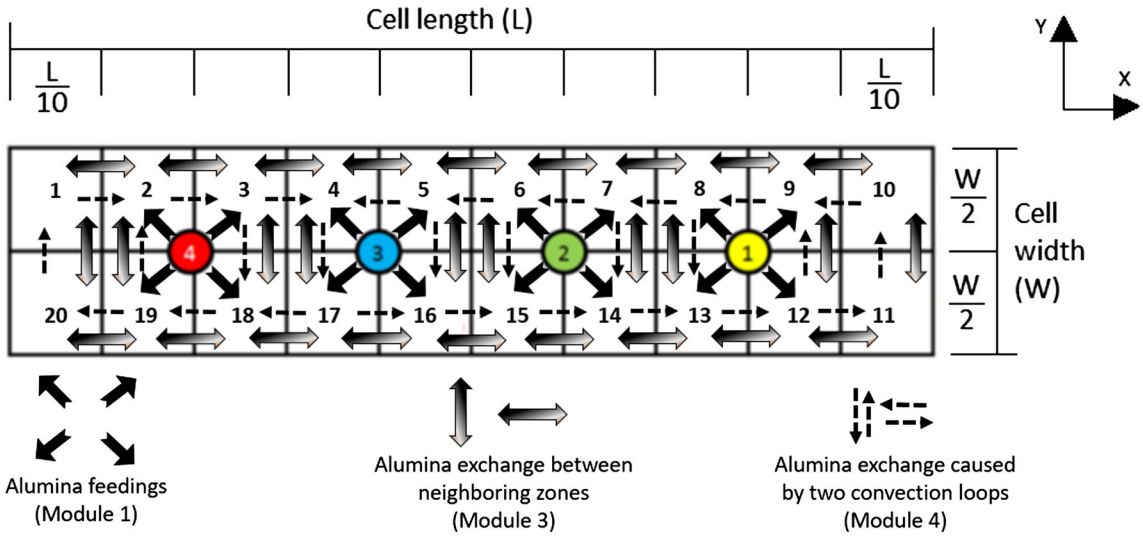


Fig. 2—Anodic assemblies, alumina feeders' positions and alumina exchange between the different zones.

$$\Delta t \leq \frac{(\Delta x)^2}{n \cdot D_{eq}}. \quad [7]$$

## V. ALUMINA DISTRIBUTION

The respective position of each feeder according to the different anodic assemblies is presented in Figure 2, along with the different exchange module described in this paper.

## VI. ALUMINA FEEDING (MODULE 1)

The first module of the simulator takes into consideration any alumina addition injected by the feeders.

The feeding strategy considered is similar to the one of an operating electrolysis cell. For instance, each feeder distributes a constant amount of alumina (approximately 1 kg) with each dose following a specific sequence and a regulated time between the doses according to the desired character of feeding (overfeeding, theoretical feeding, or underfeeding). A dose of alumina is not added to the electrolytic bath as a single shot within a single time step but rather injected over several seconds to correctly represent the reality. Experiments performed by Tessier *et al.*[22] indicated that a longer drop time will lead to improved cell stability. However, the standard feeder's design has a relatively short drop time of 1.5 seconds.[22] Moreover, in the model, the alumina is divided uniformly into the four regions adjacent to each respective feeder. For example, if 1000 g of alumina is added by feeder #1 over a period of 10 seconds, the amount of undissolved alumina in sections 8, 9, 12, and 13 would increase by 25 g for every second of the dosage.

The feedings are performed in a specific sequence based on the feeding strategy of an operating cell. At the beginning of the feeding sequence, there is a preliminary period without feeding, and then feeder #1 will always be the first one to feed, followed by feeder #3, feeder #2, feeder #4 and it returns to feeder #1 for another cycle. The time between consecutive feedings is uniformly spaced according to the feeding period. Therefore, if the cell's feeding cycle is 60 seconds, then in every 15 seconds one of the four feeders will feed. As an example, a transition from overfeeding to underfeeding is presented in Figure 3. In rare cases, it is possible that the same feeder is activated twice in a row, which explains the need for the preliminary period without feeding to avoid overlapping of two doses.

## VII. ALUMINA DISSOLUTION (MODULE 2)

Within each of the twenty discrete volumes, the alumina can be present in two distinct states: undissolved or dissolved. This module was developed to represent the mechanism that allows the alumina to go from undissolved state to the dissolved state accurately.

In each distinct region, the total amount of undissolved alumina is considered as a single alumina clump no matter the original provenance of the alumina (direct injection during feeding, convective currents, *etc.*). This clump of alumina is considered spherical and the radius of the sphere is calculated based on the volume of a sphere which englobes the overall weight of alumina with its bulk density of 1 g/cm$^3$.

Then, the alumina dissolution rate is calculated in each region for every time step based on Eq. [8], where $(dm/dt)$ (kg/s) is the dissolution rate of the alumina, $(K_m)$ (m/s) is the dissolution coefficient, $(A)$ (m$^2$) is the area of the undissolved alumina exposed to the bath, and $(C_s)$ (kg /m$^3$) is the saturation concentration of alumina in the bath calculated using the formula (Eq. [9]) developed by Skybakmoen *et al.*[23] This formula is based on the bath temperature $(T)$ (°C) and two coefficients ($\alpha$ and $\beta$) which are dependent on the different additive's

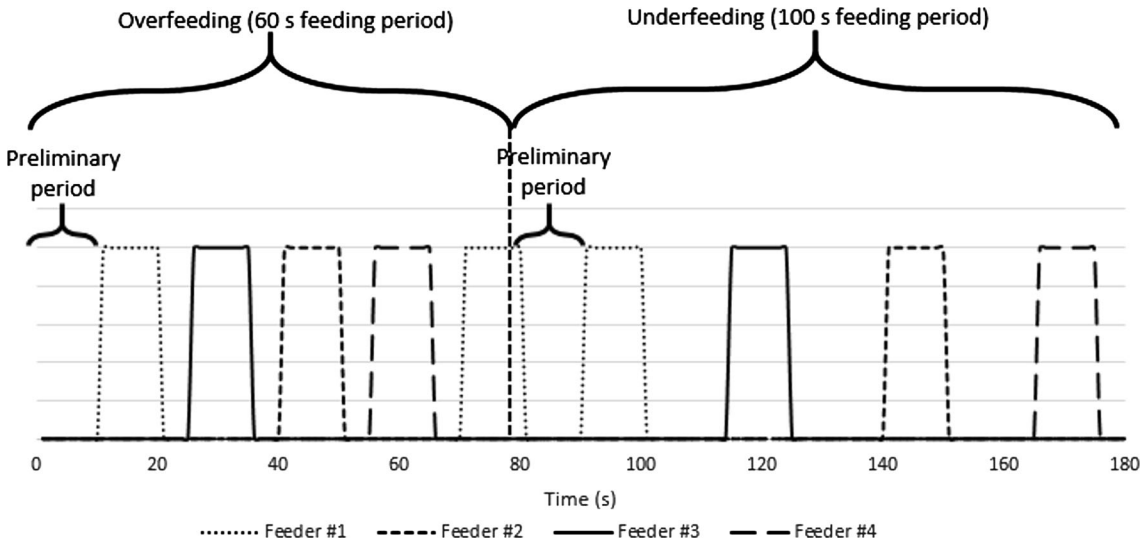


Fig. 3—Illustration of the feeding sequence during a change in the feeding cycle.

**Table I. Different Dissolution Coefficients Estimated from Published Literature**

| Study | Zhan *et al.*[20] | Wang[24] (Fast Dissolving Alumina) | Wang[24] (Slow Dissolving Alumina) | Welch and Kuschel[25] (Fast Dissolving Alumina) | Welch and Kuschel[25] (Slow Dissolving Alumina) | Average Dissolution Coefficient |
|---|---|---|---|---|---|---|
| Approximated dissolution coefficient ($K_m$) (m/s) | $2.95 \times 10^{-2}$ | $2.36 \times 10^{-4}$ | $1.06 \times 10^{-4}$ | $2.35 \times 10^{-4}$ | $3.75 \times 10^{-5}$ | $6.02 \times 10^{-3}$ |

concentration in the bath. Finally, ($C$) (kg/m$^3$) is the bulk concentration of alumina in the region surrounding the undissolved alumina clump.

$$\frac{dm}{dt} = -K_m \cdot A \cdot [C_s - C] \quad [8]$$

$$C_s = e^{\left[\alpha+\beta\cdot\left(\frac{1000}{T}-1\right)\right]}. \quad [9]$$

The dissolution coefficient has been defined based on results from the literature. By considering the dissolution curves published by Zhan *et al.*,[20] Wang,[24] and Welch and Kuschel,[25] it was possible to approximate the dissolution coefficient (presented in Table I) from these studies for various types of alumina. In the simulator, the mean value for all these five scenarios was used. However, this dissolution coefficient is only an approximation of the real conditions and increased accuracy could be obtained by determining a dissolution coefficient specific for the technology. Moreover, $K_m$ should be re-evaluated if important changes are expected regarding the alumina properties such as the particle size distribution and shape or the raw content of alpha and gamma alumina, which will affect the efficiency of the dissolution. Finally, the effect of the superheat and bath composition should also be taken into consideration when evaluating the dissolution coefficient.

## VIII. ALUMINA TRANSPORT BETWEEN THE DIFFERENT VOLUMES

Alumina is transported within an electrolysis cell by three different mechanisms (discussed in more details below):

- molecular diffusion caused by different concentration gradients in the bath
- mixing caused by the rising bubbles generated under the anodes
- large-scale convective loops in the bath caused by the magnetohydrodynamics (MHD) forces acting on the cell.

All these mechanisms were considered during the development phase of the simulator and specific modules were designed to represent correctly these phenomena.

### A. *Mass Transfer Between Neighboring Volumes (Module 3)*

Diffusion across the electrolyte is a slow process in comparison to the MHD-generated movement. Nonetheless, this phenomenon is important for the model accuracy as the importance of diffusion increases in opposition to a reduction of the MHD forces within the cell. Therefore, if the simulator is used to investigate hypothetical scenarios with low or no MHD forces,

consistent results with respect to theoretical considerations are still expected.

The rate of mass exchange between neighboring anodes is described quantitatively by a linear "driving force/rate of transfer" type correlation (Eq. [10]). The driving force of the alumina transfer is the concentration gradient approximated by $(\Delta C/L)$ [(kg/m$^3$)/m] in the equation. While $(m_{i,j})$ (kg/s) is the mass transfer rate between two adjacent volume, the proportionality factor of "generalized conductance" takes into account the section $(A_{ij})$ (m$^2$) available for the mass exchange and the so-called "equivalent diffusivity" $(D_{eq})$ (m$^2$/s). The latter englobes several mechanisms such as the molecular diffusion and the more important turbulent mixing caused mainly by the bubbles.

$$\dot{m}_{i,j} = -D_{eq} A_{ij} \frac{(C_i - C_j)}{L}. \qquad [10]$$

There is little information available in the literature about the molecular diffusivity of alumina in the molten electrolyte. Furthermore, we do not have any quantitative data about the equivalent turbulent diffusivity in the bath. For this reason, we estimated the value of $D_{eq}$ from the hypothesis of having a homogenization time of 30 minutes. The homogenization time is the duration needed to reach a concentration uniformly spread across all zones within $\pm$ 1 pct after an initially uneven distribution (illustrated in Figure 4). With this hypothesis, the corresponding equivalent diffusion coefficient could be estimated as 3.7 m$^2$/s. Figure 5 illustrates the diffusion of the alumina with the appropriate transport coefficient. It is possible to observe that after 1800 seconds, the concentrations of all regions of the cell are between 3.96 and 4.04 pct wt. Only half the cell is represented in the figure due to symmetry.

### B. *Mixing Caused by Bubbles*

Bubbles are an important driving force in the mixing of the alumina.[19,26–28] However, this phenomenon is occurring more importantly on a localized level (under the anodes) and will be beneficial for the alumina dissolution and for local transport of the dissolved alumina. The mixing caused by the bubble is taken into consideration within the alumina dissolution module (indirect effect on the $D$ coefficient) and the diffusion module as well (direct impact on $D_{eq}$). For this reason, no specific module was developed to consider the complex behavior of bubble mixing associated with alumina transport.

### C. *Cell-Scale Convection Loops (Module 4)*

During normal electrolysis, the high current of the cell leads to the generation of strong magnetic fields. All the cell conductors (risers, anode beam, busbars, *etc.*) are designed to minimize the influence of the magnetic field on the movement of the aluminum pad but MHD-generated loop are still present in the cells. These MHD forces, added to the drag force exerted between the aluminum pad and the electrolytic bath, will create a movement of the bath that can affect significantly the movement of the dissolved alumina as demonstrated theoretically[19,21,28] and experimentally.[27,29]

In this study, the movement generated by the magneto-hydrodynamic forces is not calculated by the simulator. Instead, the pattern of the electrolytic bath flow is considered similar to the results published by Hofer[21] as part of his Ph.D. thesis. The work of Hofer was performed on a similar cell technology and similar cell amperage what we used for the simulator. As illustrated in Figure 6, the mass exchange between the different volumes caused by bath movement is asymmetrical as observed experimentally in a previous work by the current authors.[29] The speed of the bath across the different respective volumes was also determined based on the Hofer's research with maximum values located in the corners of the cell with a magnitude of approximately 8 cm/s.

Strong refinements to the simulator could be obtained by performing an MHD simulation specifically for the cell technologies considered and applying the results in a similar way to the simulator.

During the convective movement of the electrolytic bath caused by MHD dynamics, both dissolved and undissolved alumina will be carried in the electrolyte flow and eventually move from one section of the cell to an adjacent zone. It is the only mechanism considered in the model that can transport undissolved alumina to regions of the cell non-adjacent to an alumina feeder. However, a ratio can be used to limit the transport rate of the solid alumina if required. Alumina clumps are known to float on top of the electrolytic bath as a raft.[30,31] Therefore, if the alumina clump is important, it is assumed that it will transfer less rapidly due to friction between the alumina raft and the anode cover material. No information in the literature was available to identify this ratio so this value had to be determined arbitrarily based on an engineering judgment. This value was set to 10 pct.

## IX. ALUMINA CONSUMPTION (MODULE 6)

During electrolysis, alumina is consumed with a specific rate determined by the respective current passing through each zone and the average current efficiency of the cell. The alumina consumption rate can be calculated for every time step using Eq. [11] based on Faraday's law of electrolysis, where $(m_i)$ (g) is the respective amount of alumina consumed, $(I_i)$ (A) is the amperage going through a specific section of the cell, $(t)$ (s) is the time step, (M) (g/mol) is the molar mass of the alumina, $(F)$ (C mol$^{-1}$) is the constant of Faraday, $(z)$ (–) is the valency number of ions required for the alumina to react, and $(CE_i)$ (pct) is the respective current efficiency of the section. At the current state of the simulator, the current efficiency is considered as constant for every section but further refinements could consider localized current efficiency, more importantly for regions demonstrating a high risk of LVAE, thus a high risk of local instability.

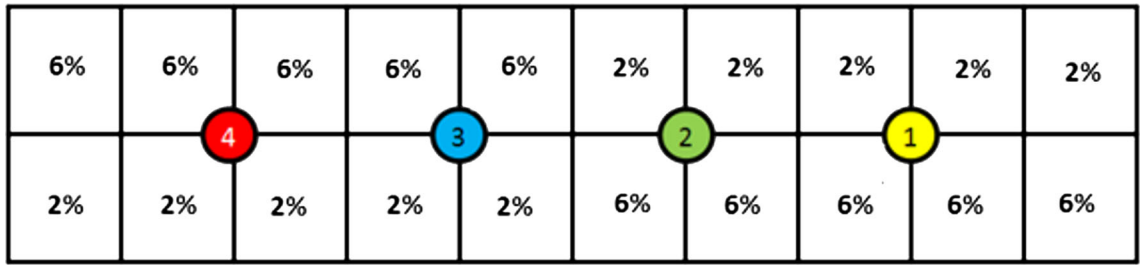


Fig. 4—Theoretical scenario used to determine the appropriate transport coefficient.

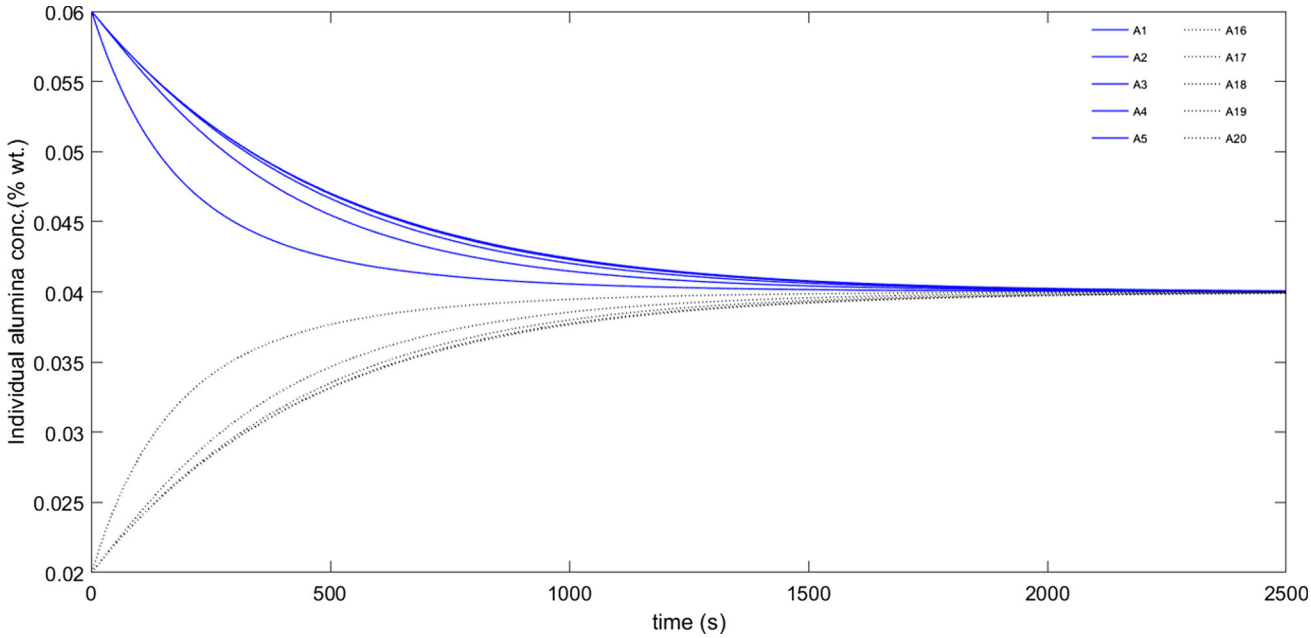


Fig. 5—Impact of the diffusion on the alumina concentration of the different zones for a theoretical scenario with $D_{eq}$ = 3.7 $m^2/s$. 10 zones are represented by a different curve.

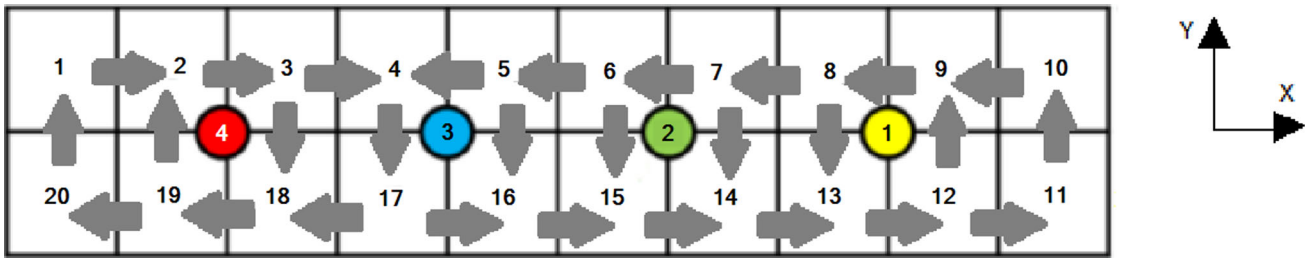


Fig. 6—Exchange between the different volumes based on the work from Thomas Hofer.[21]

$$m_i = \frac{I_i \cdot t \cdot M}{F \cdot z} \cdot \mathrm{CE}_i. \qquad [11]$$

Having calculated the individual consumption rate of the alumina for each section of the cells, the mass of produced aluminum can be calculated for each time step as an additional indicator of the cell's local performances.

Finally, a low threshold in the alumina concentration was defined arbitrarily as 0.02 pct wt. In the rare occurrence where the alumina concentration for specific regions gets below this threshold, the current is distributed to other regions of the cell and the alumina concentration will not decrease further to eliminate the risk of obtaining negative alumina concentration. In the unexpected occurrence where all regions of the cell would reach this threshold, no calculation of the aluminum production would be possible until the alumina concentration increases back to value above

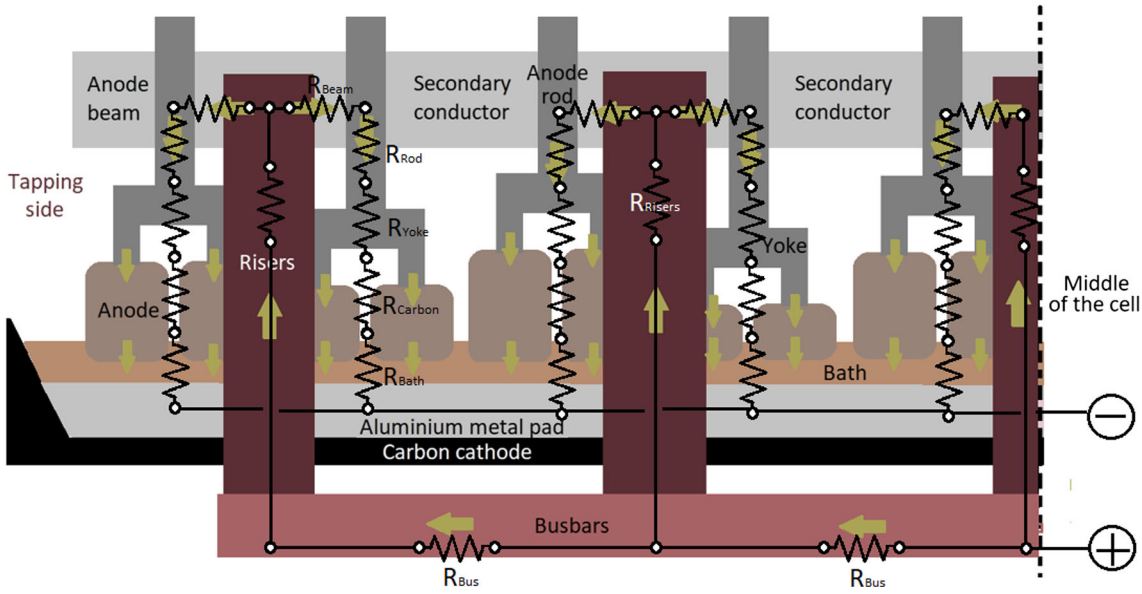


Fig. 7—Various elements considered as part of the electrical network.

this limit; therefore, the simulator's modules 5, 6, and 7 would be skipped and the cell is considered under high-voltage anode effect.

## X. ELECTRICAL CURRENT DISTRIBUTION MODULE (MODULE 5)

In the electrolysis cell, all twenty-anodic assemblies are connected parallel to each other. Therefore, the current is free to reorganize constantly to choose the path of the lowest overall resistance. This module was designed to adequately represent the entire cell conductors as well as the different resistance from the electrolysis bath in a simplified electrical model which runs for every time step.

## XI. CELL RESISTANCE MODULE

The electrical network used to represent the cell's conductors was simplified to consider exclusively the principal conductors of the electrolysis cell. The primary conductors considered in the resistance network are illustrated in Figure 7. They start at the middle busbar junction between the previous and the simulated cells and goes sequentially through the busbars, the risers, the anodic assemblies, and the electrolytic bath all the way to the aluminum metal pad. There is no need to consider any further elements such as cathodic resistance due to the possible reorganization of the current occurring in the highly conducting aluminum metal pad.

Some secondary conductors (shown in Figure 7) are present on a normal operating cell but no current is supposed to go through them under conditions close to the normal operation. They are, however, beneficial for the cell mechanical stability and also help the current equilibrium during high current instabilities such as HVAE. These secondary conductors were not considered in the model due to the significant increase in complexity that they would have required while offering very low improvements to the results.

## XII. INDIVIDUAL RESISTANCE OF THE ANODIC ASSEMBLIES

In addition to the electrical conductors, some specific elements must be considered for each individual component of the anodic assemblies. For this reason, individual resistance specific to anode position are the results of five resistances connected in series. These five resistances and any respective considerations are described in the following sections.

### A. *Resistance of the Anode Beam Conductor*

The resistance of this element is calculated similarly to the other electrical conductors (busbars ($R_{\text{Bus}}$), risers ($R_{\text{Risers}}$), and transversal bars) using Eq. [12], where ($R$) ($\Omega$) is the calculated resistance, ($\rho$) ($\Omega$ m) is the electrical resistivity of the conductor, ($L$) (m) is the length of the conductor, and ($A$) (m$^2$) is the area of the surface of the conductor.

$$R = \frac{\rho \cdot L}{A}. \qquad [12]$$

### B. *Resistance of the Anode Assembly*

The anode assembly is composed of three resistance elements, the anode rod, the carbon, and the yoke connecting both these elements. Based on the work of other researchers[32] for the same cell technology, it was possible to define a constant resistance value for the yoke ($R_{\text{Yoke}}$). This resistance considers the yoke electrical network as well as the contact resistance in the

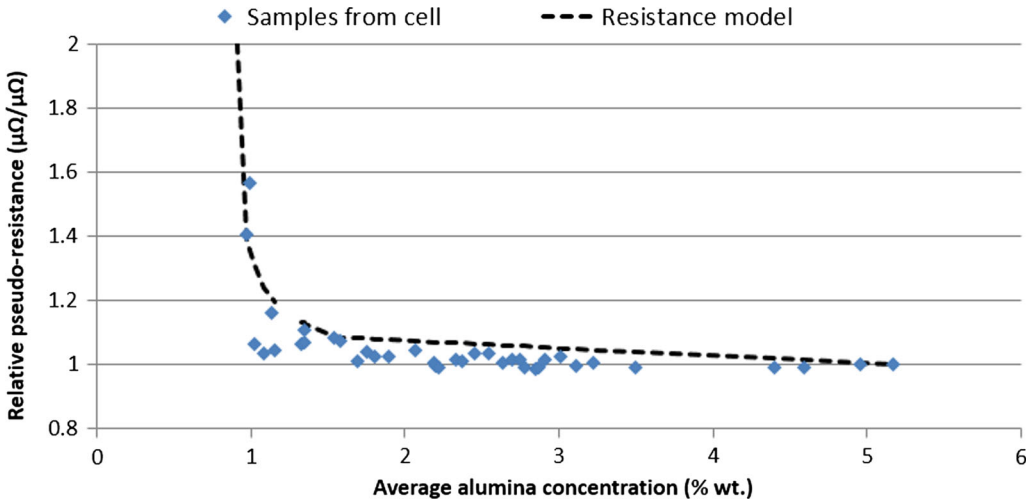


Fig. 8—Effect of the average alumina concentration in a cell on its pseudo-resistance.

anodic "clad" and the contact resistance associated with the cast iron connections. However, further improvements to the model could also include the effect of the temperature during the current ramp up as well as when the yoke gets closer to the electrolytic bath.[32]

The anode rod ($R_{\text{Rod}}$) and the carbon resistance ($R_{\text{Carbon}}$) are also calculated as electrical conductors (Eq. [10]). However, for each anodic assembly, the anode rod and the carbon length will be different depending on the anode position within the anode changing cycle. The respective length of each anode rod ($L_{\text{ROD}}$) (m) and carbon ($L_{\text{C}}$) (m) is calculated by considering a constant length ($L_{\text{TOT}}$) (m) between the anode beam and the bottom of the anodic assembly. Then, as the initial carbon height of a new anode ($L_{\text{INI}}$) (m) is known, the length of carbon for each anodic assembly can be identified by subtracting the respective carbon erosion which depends on the total number of days ($N$) (days) since the anode was planted in the cell. The daily consumption of carbon ($C_{\text{CONS}}$) (m/day) is measured frequently at the smelter and the information was provided by the smelter for this study. Details of the calculation explained hereabove are presented in Eqs. [13] and [14].

$$L_{\text{c}} = L_{\text{INI}} - N \cdot C_{\text{CONS}} \qquad [13]$$

$$L_{\text{ROD}} = L_{\text{TOT}} - L_{\text{c}}. \qquad [14]$$

## C. *Resistance Across the Electrolytic Bath*

Three elements should be considered to adequately represent the resistance corresponding to the electrolyte: the Ohmic resistance of the bath and the additional apparent resistances caused by the overvoltage and the excess resistance due to the presence of the bubbles at the bottom of the anodes. Therefore, these elements were considered in Eq. [15], where ($R_{\text{Bath}}$) (Ω) is the resistance of the electrolyte, ($\rho_{\text{bath}}$) (Ω m) is the electrical resistivity of the bath, (ACD) (m) is the interpolar distance, ($A_{\text{bath}}$) ($\text{m}^2$) is the surface area of the anode bottoms of an element, and ($F$) (–) is a factor ($F \geq 1$) used to represent the combined amplifying effect of the overvoltage and the bubbles.

$$R_{\text{bath}} = \frac{\rho_{\text{bath}} \cdot \text{ACD}}{A_{\text{bath}}} \cdot F. \qquad [15]$$

In the previous equation, two elements are dependent on the local conditions within the cell. Firstly, the resistivity of the bath is determined by Eq. [16], originally presented by Wang *et al.*,[33] where ($\sigma$) (S/cm) is the electrical resistivity of the bath, BR (–) is the bath ratio of the electrolyte, ($T$) (K) is the absolute bath temperature, and ($Al_2O_3$, $CaF_2$, $MgF_2$, LiF, $Al_4C_3$) (pct wt) are the respective concentration of each component. Therefore, an uneven alumina concentration in the bath will generate different individual resistance.

$$\begin{aligned} \ln \sigma = {} & 1.7738 + 0.3351 \cdot \text{BR} - 21.3 \\ & * 10^{-3} \cdot \text{Al}_2\text{O}_3 - 17.5 * 10^{-3} \cdot \text{CaF}_2 \\ & - 32.1 * 10^{-3} \cdot \text{MgF}_2 + 27.3 * 10^{-3} \cdot \text{LiF} \\ & - 121.1 * 10^{-3} \cdot \text{Al}_4\text{C}_3 - 1.5337 * 10^3 / T \end{aligned} \qquad [16]$$

Secondly, the minimum value of the ($F$) factor (under saturated bath) was determined to be 1.1212 according to Grjotheim *et al.*[34] Further increase in this ratio was defined empirically based on an experimental study in Alouette's smelter. The measurements carried out to develop the empirical model are illustrated in Figure 8. It demonstrates that the resistance increases drastically when the alumina concentration leans toward zero which is caused by the combined effect of overvoltage and a significant layer of resistive gas (PFC) under the anodes.

## XIII. RISK OF LOW-VOLTAGE ANODE EFFECTS (MODULE 7)

Previous research by the current authors[18] demonstrated that the standard deviation among individual anode currents is the strongest indicator of LVAE. Therefore, it is easily possible to calculate the standard deviation of the individual anodic currents resulting from the simulator to predict the risk of LVAE. Experimental measurements demonstrated that the standard deviation threshold was equivalent to 3.65 kA.[18]

To correctly implement this threshold in the simulator, it was necessary to determine if the resulting standard deviation from the simulator was within the same order of magnitude as the real electrolysis cell. Under normal operations, the simulation results are more than three times lower in terms of standard deviation among individual anode currents than the real measurements for similar conditions. This difference can be attributed to the uncertainty associated with the distance between each respective anode and the metal pad, *i.e.*, individual anode-cathode distance (ACD). Under the industrial practice, there are small variations (few mm) attributed to the positioning of the anodes when inserted into the cell. Moreover, the uniformity of the aluminum metal pad is not necessarily consistent over the entire surface. For example, the magnetic field can shift the current closer or further to some anodes depending on the positions. These considerations, combined with the different type, and level of instability can generate movement of the metal pad which will inherently change the local ACD of each anode. These elements cannot be accurately represented by the simulator due to the irregularity of these events. Consequently, by considering that the ACD is constant for each anode in the mathematical model, the small ACD variations from anode to anode in the real cells can explain the observed deviation. The effect of these variations is even more important due to the very small ACD[35] of this specific smelter. Finally, the threshold value in the mathematical model was adjusted according to this observation.

## XIV. VALIDATION OF THE SIMULATOR

### A. *Experimental Setup*

To validate the simulator, four different alumina feeding scenarios were generated in the cell to create alumina concentration gradients in the electrolytic bath. For all scenarios, the alumina supplied to the cell was reduced by turning off certain feeders. However, the position of the stopped feeders was changed depending on the scenarios. During these test, individual anode current was monitored continuously with the system provided by the aluminum smelter. Furthermore, the cell's gas composition was also continuously monitored and bath samples were taken periodically for analysis of the alumina concentration. The four different scenarios investigated are presented in Table II. These scenarios were designed to deplete the overall alumina concentration in order to obtain LVAE in cells, within a reasonable amount of time (approximately 1 hour) while avoiding HVAE for as long as possible. The different locations of the feeders were chosen to assure that the model was consistent for symmetric and asymmetric scenarios. Finally, in the case of scenarios 1 and 4, the tests had to be slightly modified to avoid disrupting the normal operations of the electrolysis process (*i.e.*, anode change schedule).

### B. *Following the Alumina Concentration*

To investigate the change in alumina concentration within the cells, samples of the electrolytic bath were extracted periodically in six different positions illustrated in Figure 9 using a sampling probe to obtain conical shaped samples. Prior to every test ($t = 0$), one sample in each of the six locations was extracted to determine the initial conditions for the simulator. Then, the time lapse between each sampling was always 10 minutes or less and three samples were always taken almost simultaneously ($\pm$ 30 s). The three samples were extracted in order to obtain information on the concentration gradient along the longitudinal direction ($x$-axis) of the cell. In alternation, the 3 samples along the $x$-axis of the cell were taken on opposite sides of the $y$-axis. Analysis of the alumina concentration was performed on site at the Alouette smelter's laboratory using the ALCAN method.

### C. *Gas Composition Monitoring*

The gas was extracted using stainless steel sampling probes directly from each of the five inner ducts that route the gas from the different parts of the cell up to the main exhaust duct in order to well represent the overall cell.[36] The flow rate of each probe was regulated to 1 LPM and the total gas flow (5 LPM) was routed to a GASMET™ DX-4000 FTIR (Fourier Transformed Infra-Red) spectrometer using a Peltier-cooled

**Table II. Information Related to the Validation Scenarios Investigated**

| | Feeder 1 | Feeder 2 | Feeder 3 | Feeder 4 | Duration (s) |
|---|---|---|---|---|---|
| Scenario #1-A | Stopped | Stopped | Active | Active | 0 to 4080 |
| Scenario #1-B | Stopped | Stopped | Stopped | Stopped | 4080 to 5700 |
| Scenario #2 | Active | Stopped | Stopped | Active | 0 to 4620 |
| Scenario #3 | Active | Active | Stopped | Stopped | 0 to 5400 |
| Scenario #4-A | Stopped | Active | Active | Stopped | 0 to 4020 |
| Scenario #4-B | Active | Active | Active | Active | 4020 to 4320 |

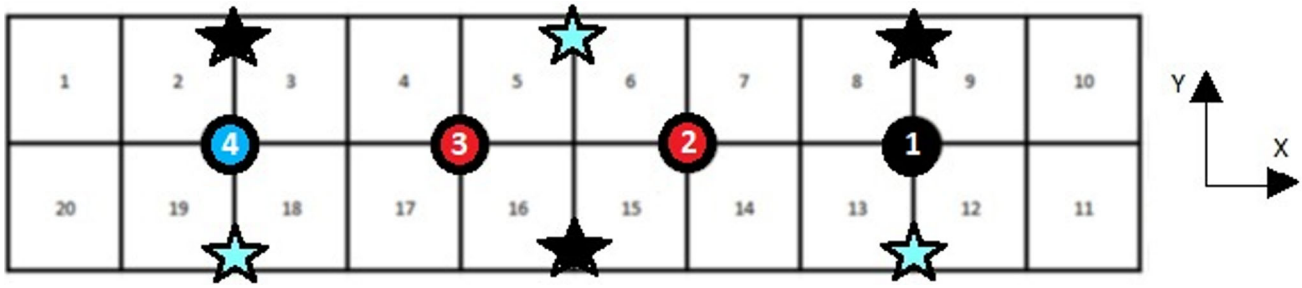


Fig. 9—Extraction point (stars) for bath samples during the test. Stars with the same colors represent areas where the bath was sampled simultaneously.

mercury-cadmium-telluride detector (sample cell path: 9.8 m, volume: 0.5 L, resolution: 7.8 $cm^{-1}$). The gas stream was sent sequentially through the desiccant, activated alumina, a 5-mm filter, and finally a 2-mm filter to remove traces of water, hydrogen fluoride, and dust, respectively, for the protection of the measuring equipment. The gas was preheated to 120 °C before entering the FTIR and concentration measurements were performed at a rate of 10 scans per second. Average values for 20 second periods were recorded. The background spectrum was redefined using high-purity nitrogen prior to every test.

### D. *Validation of the Cell Voltage*

A first element to be evaluated is the accuracy of the simulator to reproduce the behavior of the overall cell voltage; therefore, a scenario with different feeding periods was observed in the real electrolysis cell and reproduced in the simulator. As illustrated in Figure 10, the long-term tendencies of typical voltage variations in cell voltage provoked during different feeding periods can be adequately represented by the simulator. However, the mathematical model was not designed to represent cell events with a higher frequency such as the movement of the bubbles or cell instabilities caused by the movement of the metal pad or anode incidents (spikes). Additionally, some discrete events like the movement of the crust breaker can also perturb the cell voltage as it locally and randomly increases the gas flow out of the electrolytic bath. Despite neglecting certain events, changes in the global ACD of the cell can be represented well with the simulator. However, the actual movement of the anode beam had to be approximated in this study. More detailed results can be expected if the anode beam movements were monitored and measured precisely in terms of ''distance traveled (mm)'' instead of ''total time of travel (s).''

### E. *Validation of the Alumina Distribution*

As mentioned previously, four scenarios were planned and the deviations between the simulated results and data series taken from the monitored cell were evaluated. The results of the simulation with the initial hypotheses discussed in the previous section of this paper are presented in Figures 11(a) through (d). For each figure, the data resulting from the simulator are the average alumina concentration predicted for each element of the cell. Hence, the blue line represents the average for the duct end side, the red dashed line is the average for the center region, and the black dotted line is the average concentration on the tapping side. The results demonstrate that the general behavior is well represented by the simulator. However, there is more uniformity across the different regions of the cell in the simulator than there is in the real cell. This lack of agreement can be caused by a too strong coupling (high value of the exchange factor) between the different elementary volumes. This exchange factor is primarily dependent on the bath velocity in the cell. As a matter of fact, the average bath velocity from the simulator was estimated using the results of an external study.[21] Even if the study performed by Hofer had many similarities with the investigated cells, some differences may cause the actual bath velocity to be smaller than predicted numerically. For this reason, an optimization was performed using the data collected during the validation, and as a result, a reduction of 60 pct was imposed on the bath velocity used in the simulator. The corrected results are presented in Figures 11(e) through (h).

The corrected results demonstrate a better agreement with the real measurements, especially in the cases where there was an asymmetry in the alumina feeding (cases 1 and 3). Under these scenarios, the measured alumina concentration shows a higher range of values. Therefore, as the corrected bath velocity reduces the overall cell mixing, it describes better the cell's inhomogeneity leading to a closer agreement between the simulator and the reality. In its current state, the simulator cannot reproduce the unpredictable fluctuations in the alumina additions coming from random sources such as the effect of anode cover material or the recuperation of alumina from the sludge located below in the aluminum pad. Important instabilities in the cell (e.g., during high-voltage anode effect) may provoke significant reoxidation of the aluminum metal pad for short amount of time, which, in turn may generate significant alumina additions to the electrolytic bath. This phenomenon was previously observed by the authors[29] when the cell's conditions reach LVAE or HVAE. In the current study, we can observe this phenomenon at the end of scenario #3 where there is a significant increase (half a percent) in the alumina concentration at both extremities of the cell even if no additional alumina feeding was provided by the cell's feeders.

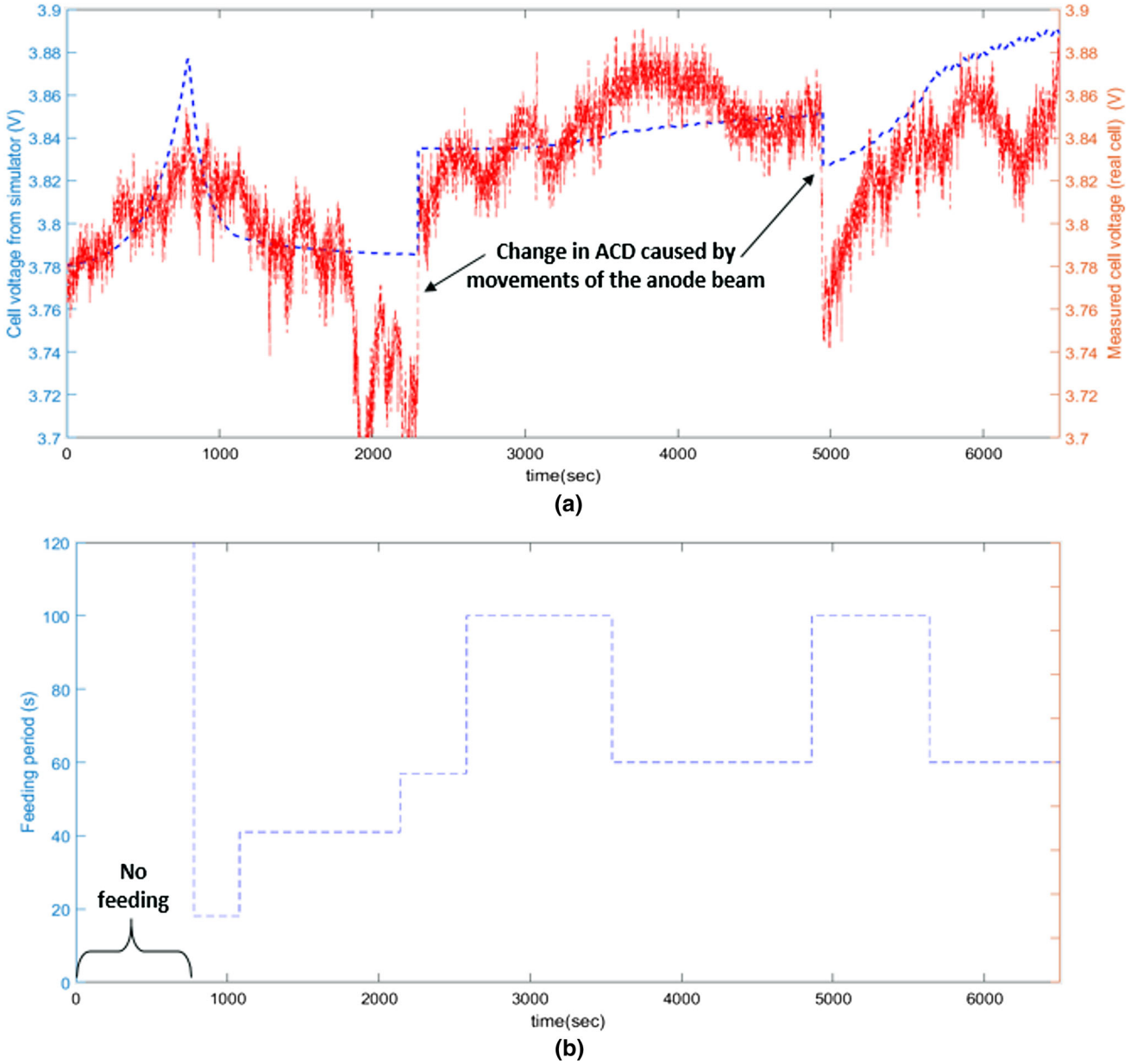


Fig. 10—Comparison of the cell voltage between the simulator (dashed line) and real measurements (continuous line) (*a*) during different feeding cycles (*b*).

### F. *Validation of the Standard Deviation Among Individual Anode Currents and Validation of PFC Emissions*

After optimization of the bath velocity, the efficiency of the simulator to predict LVAE was investigated using the standard deviation among the simulated individual anode currents. The evolution of this parameter for the four validation scenarios is presented in Figure 12, along with the standard deviation of the measured individual anode currents in the real cell. The measured concentration values of the $CF_4$ gas extracted at the duct end of the cell are also shown. The calculated standard deviations were normalized with respect to the average value of these respective parameters under normal behavior. Moreover, the measured standard deviation in the real cell showed an important noise level. For this reason, the results were smoothed using a moving average of 20 seconds. Finally, the vertical arrow in each figure represents the instant where the standard deviation threshold value was reached according to the simulator.

The evolution of the simulated standard deviation correlates strongly with the observed PFC emissions for all the scenarios investigated, demonstrating that this indicator can be used to predict occurrence of low-voltage anode effects. Interestingly, the simulator's correlation with the $CF_4$ emissions is stronger than the actual measured standard deviation. In all cases, the increase in standard deviation predicted by the simulator is obtained earlier or at the same time as the increase in

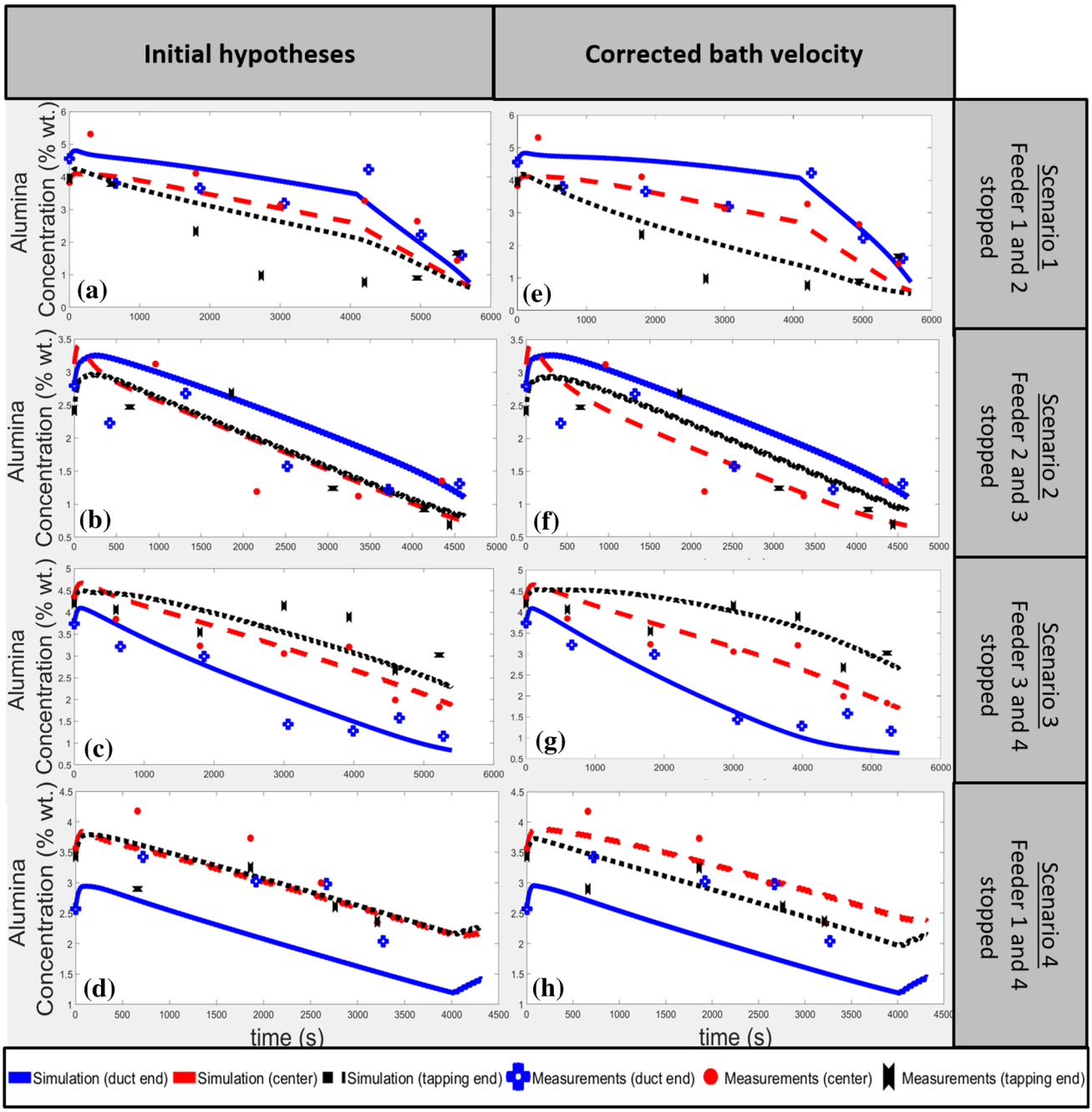


Fig. 11—Comparison of the simulated the alumina concentration history and real measurements. Figure (*a*) to (*d*) illustrates the results for scenarios 1 to 4, respectively, with the initial hypotheses. Figure (*e*) to (*h*) illustrates the results for scenarios 1 to 4, respectively, after correction of the bath velocity.

standard deviation measured by the individual current monitoring tool. This curious behavior is mainly due to some elements discussed previously that are not considered in the simulator like cell instabilities or variations in the local value of ACD. For this reason, the real cell is less sensitive than the simulator to the variations that are caused strictly by different alumina concentrations in the cell. This observation reveals that the simulator is capable to reveal information that cannot even be observed on an operating electrolysis cell, thus making it a very effective and sensitive tool to predict low-voltage anode effects.

### G. *Further Improvements and Potential of the Simulator*

The simulator satisfies its original goal as to "correctly simulate temporal and spatial variations of the alumina distribution in an electrolysis cell in order to predict low voltage anode effects." Further improvements can be achieved of the simulator to enhance its

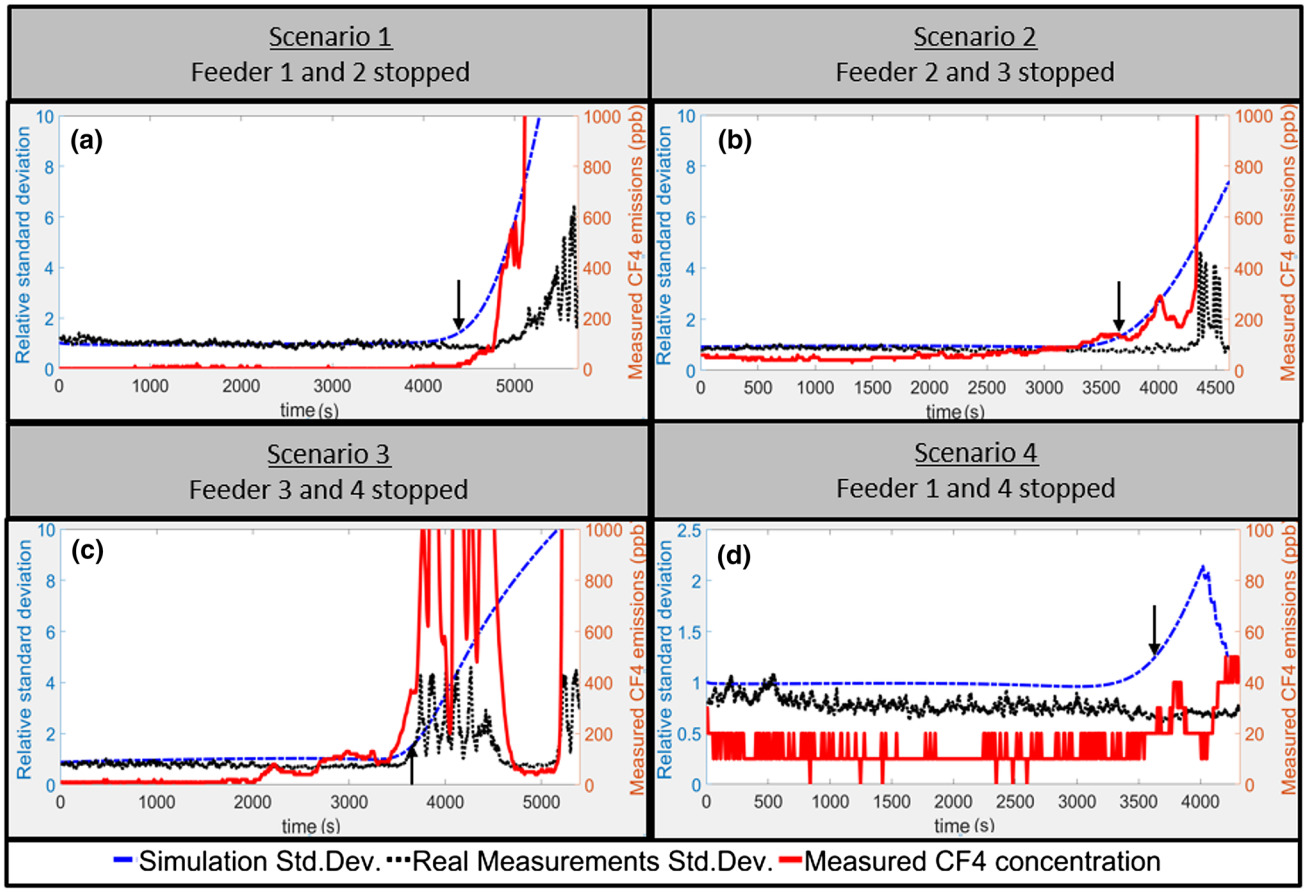


Fig. 12—Evolution of the simulated and measured standard deviation among individual anode currents during the four different validation scenarios, (*a*) to (*d*), respectively, along with the measured $CF_4$ concentration.

performance and provide more detailed results and useful information for improving the electrolysis process. Some of these improvements are as follows:

- Improvement of the fidelity of the mass exchange pattern and bath velocity flow based on the specific cell technology.
- Introduction of metal pad instabilities that influence the local ACD in time.
- Current efficiency should vary in time depending on the actual state of the process, leading to higher rate of metal reoxidation during LVAE or HVAE.
- Introducing a sink/source of alumina to represent the formation and dissipation of sludge below the metal pad.
- Incorporation of the energy balance in the mathematical model to follow the formation of hot or cold regions leading to different dissolution efficiencies.

However, even in its current state, the simulator can be used efficiently to investigate and improve some elements of the electrolysis process as demonstrated in the next section.

### H. *Using the Simulator to Improve the Electrolysis Cell Process*

Using the alumina distribution simulator can also be beneficial to increase the understanding of some elements influencing the electrolysis process, which might lead to improvements of the cell stability and increased metal production. Investigations are presented in the next sections of this paper and the described results provide useful information as well as possible refinements on the electrolysis process.

#### 1. *Analysis of the effect of the conductors*

Due to the important size of the electrolysis cell, the electrical network carrying the current is similar but not exactly the same depending on the anode positions. Therefore, the anticipated difference in current can be

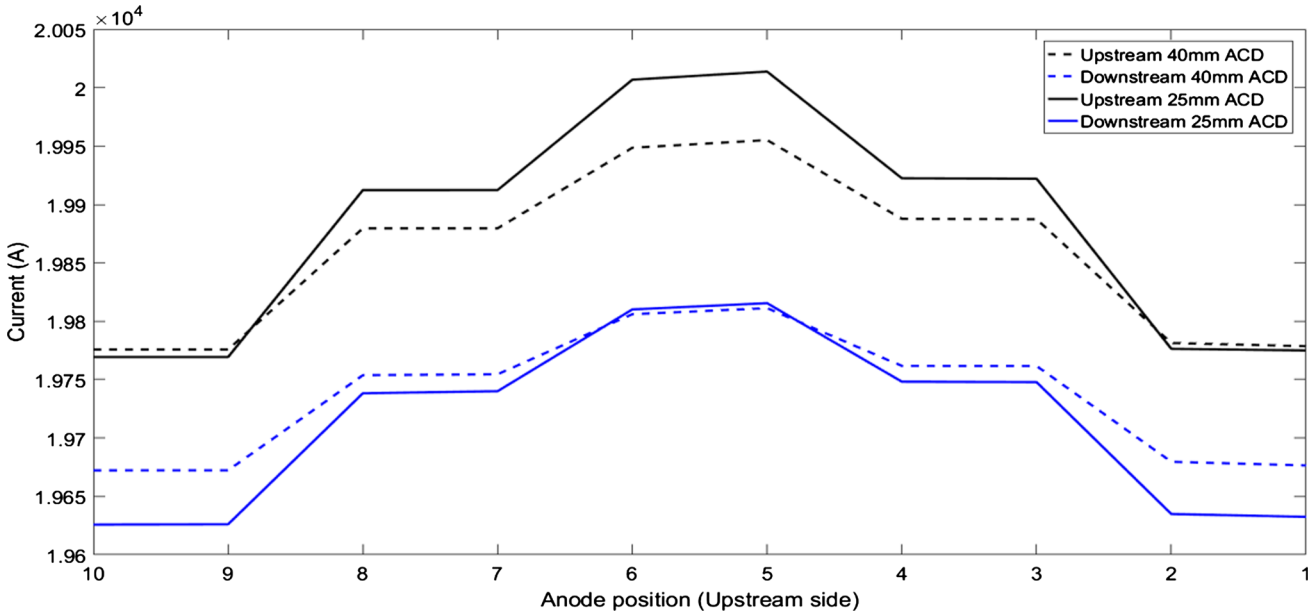


Fig. 13—Current distribution in the cell for similar anode conditions and different ACD.

evaluated by the simulator. Figure 13 illustrates the current distribution in a cell with identical anode assemblies, *i.e.*, with the same carbon height. Therefore, only the slight differences of the electrical resistance network prior to the anode rods will influence the current distribution. It is possible to observe a difference of 375 A between the anodes driving the most and less current only due to the differences in the electrical resistance network for an ACD of 25 mm. As the ACD increases to 40 mm, the difference between the different anodes diminishes due to the relatively high resistivity of the electrolyte. Interestingly, the figure demonstrates that when the ACD increases, the current redistributes from the region driving the most current (upstream center) to the regions that were driving the less current (downstream extremities). Consequently, only minimal change in current can be observed in the regions of the cell where the current was already close to the theoretical average current (19.75 kA).

However, the case simulated in Figure 13 is unrealistic due to the continuous anode changes that occur in a cell, leading to different heights in carbon, hence different resistances. Figure 14 is more representative of the predicted current distribution during normal operation due to the different states of carbon consumption of the individual anode assemblies. In this case, a change in ACD will lead to a similar behavior but its effect is amplified. In Figure 13, a 15-mm change in ACD leads to a maximum change in individual current of 75 A. However, a similar change in ACD with different carbon heights leads to a maximum change of 384 A. Therefore, the effect of the ACD on the local anode current can easily reach 1.3 pct/cm. This value appears insignificant for a small change in the global ACD. However, if the ACD is not consistent for the entire cell due to a deformed metal pad, the localized differences can be even more important.

On the other hand, the effect of the carbon erosion is extremely important on the individual anode current. The results demonstrate that the last anode that was changed* in the cell drives less current, due to a higher resistance caused by the carbon, while the next anode to be changed is among the ones driving the most current. In this scenario, the overall difference between the anodes driving the most and less current is 2.9 kA (Figure 14). This difference represents nearly 15 pct of the average anode assembly current. For this reason, a study of the anode change cycle would be beneficial to evaluate if areas of the cell can be more propitious to increased cell current during specific periods, which could lead to higher risk of alumina depletion and ultimately leading to LVAE or HVAE.

*The study presented in this section does not consider the effect of the current pick-up (increasing temperature and frozen bath layer) but considers exclusively the resistance network of the anode assembly.

2. *Improvement of the feeding strategy*

In scenario illustrated in Figure 15, operations under normal behavior were simulated with constant feeding from each feeder with feeding periods similar to those of a real electrolysis cell. It can be observed that there is a constant irregularity in the alumina concentration of the different zones. As expected, the zones closest to the center of the cell are constantly richer in alumina than the extremities. However, the two extremities are also different from each other due to the absence of symmetry in the alumina exchange caused by the cell-scale MHD convective loops. Therefore, at the end of the underfeeding periods, the zones at the duct end of the cell tend to have a very low alumina concentration. Knowing that these zones are not as uniform as the rest

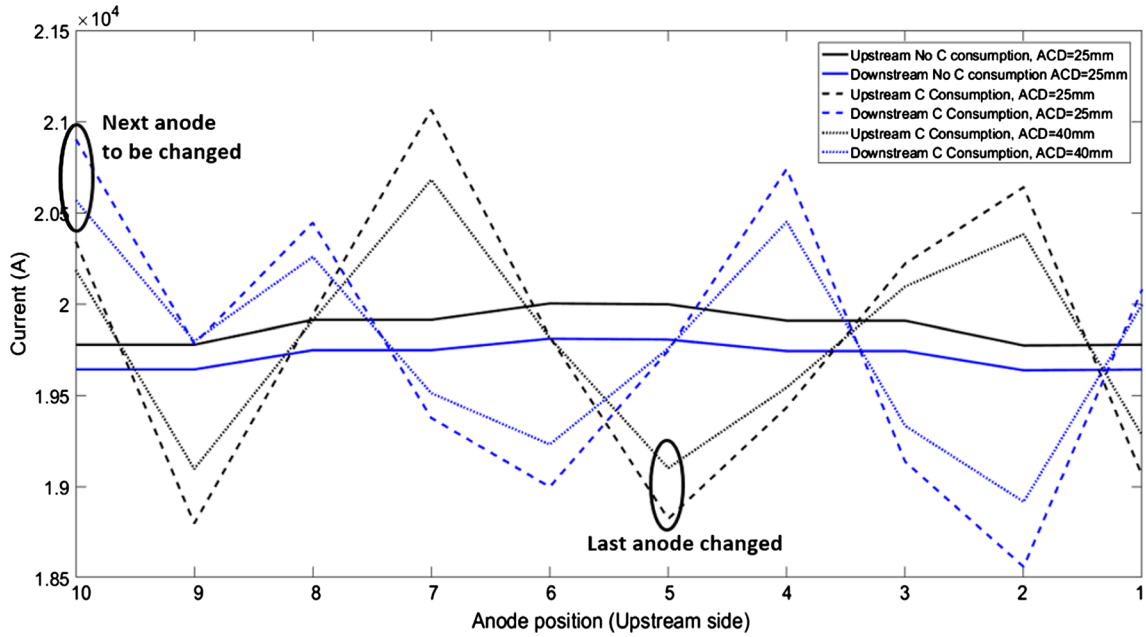


Fig. 14—Current distribution in the cell for different anode conditions and different ACD.

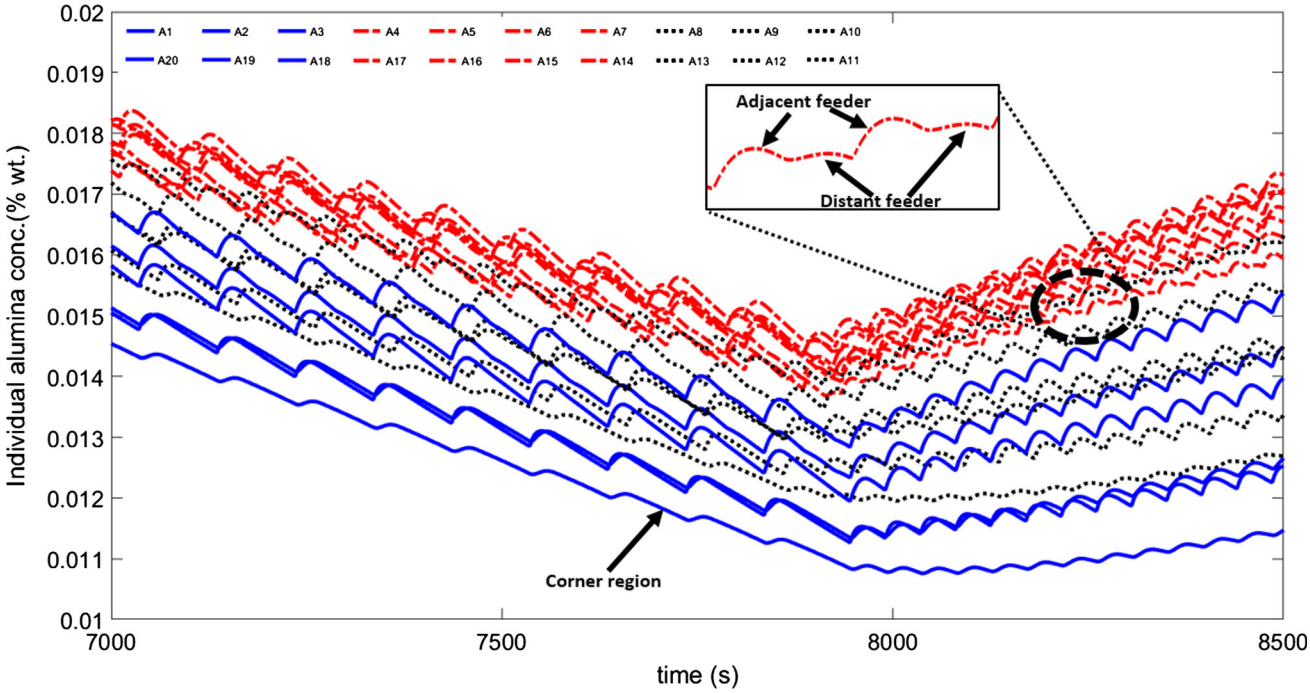


Fig. 15—Alumina concentration of the different regions at the end during the transition from underfeeding to overfeeding.

of the cell, various measures can be put into place to improve the uniformity of the alumina concentration. A plausible solution to this problem could be to increase the total amount of alumina fed by the specific feeder in this region to lean toward a more uniform distribution. However, considerations, such as changing the point feeder's action pattern, should also be taken into account to assure that this additional alumina dissolves properly in order to avoid blocking the feeder and generating more problems.

The results also clearly demonstrate that some regions of the cell receive alumina from multiple sources. In the zoomed part of Figure 15, we can see that the alumina concentration of some region varies with the feeding from the adjacent feeder as well as feedings from a distant feeder. It is possible to observe this behavior due to the transfer of undissolved alumina from one region to another. The opposite behavior can also be observed in the corner regions of the cell where a smaller amount of undissolved alumina is distributed, which leads to

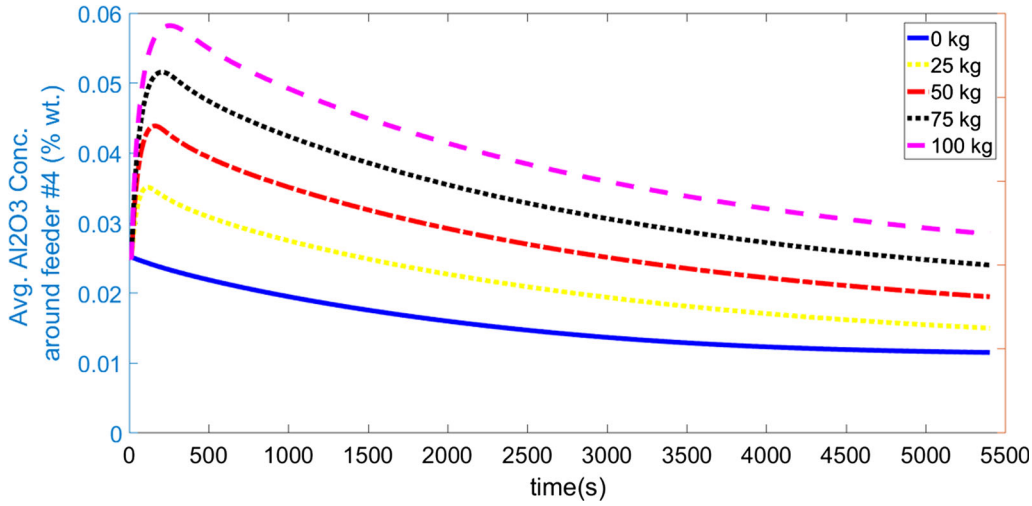


Fig. 16—Impact of stopping a feeder after an important addition of parasite alumina.

smaller amplitude in the variation of the alumina concentrations. Consequently, these regions are more likely to be at low level of alumina concentration.

3. *Analysis of the feeder stoppage after an anode change*

It is a common practice to stop for a significant period any feeders next to an anode that has undergone a procedure such as an anode change or anode covering. During these events, an important amount of alumina can be injected into the electrolyte by the anode cover material, which is a mix of crushed electrolytic bath and alumina. For this reason, the feeders are generally stopped until this parasitic alumina is dissolved and consumed. However, stopping a feeder too long can have a negative impact on the cell behavior. Using the simulator, different scenarios were investigated to provide information in order to determine the ideal duration of the stoppage depending on the smelter's specific amount of alumina added during the procedure. The results of this investigation are presented in Figure 16.

The alumina concentrations shown in the figure represent the average alumina concentration of the four zones adjacent to the stopped alumina feeder for different stoppage times and different amounts of parasite alumina fed. While a specific feeder is stopped under these circumstances, the feeding periods of the three active feeders are shortened in order to maintain the theoretical feeding rate necessary for the cell. Finally, based on the result from the previous section, the anode changed in the simulation is anode #2, which is located in the critical section of the cell (close to feeder 4) in order to illustrate the worst-case scenario for risks of anode effects.

The results presented in Figure 16 demonstrate that it is possible to determine precisely the correct duration of time that a specific feeder should be stopped if parasite alumina is anticipated, to avoid depletion of alumina, leading to anode effects or to avoid extra feeding that could lead to sludge generation. However, to use correctly this tool, a partnership with the electrolysis team (technician and engineers) is necessary to assure that the estimated parasite alumina feeding is representative of the real conditions.

Finally, the results also demonstrate that if the correct amount of alumina is provided to the cell from distant feeders, the area around the stopped feeder will eventually reach a new equilibrium concentration. In the case where no parasite alumina was provided, this new concentration is approximately 1 pct wt lower than the original cell concentration. For this reason, the risks of reaching anode effect conditions while stopping a single feeder should be minimal if the average alumina concentration was close to 3 pct prior to the stoppage. However, it is assumed that the other feeders perform optimally and that 100 pct of the dosed alumina eventually reaches the electrolysis bath, which might not always be the case, especially with an increased alumina feeding rate.

## XV. CONCLUSION

In this paper, a novel, non-homogenous approach was presented to simulate the alumina and current distribution within the bath of an electrolysis cell. With this information, it is possible to use the model to predict the onset of $CF_4$ emissions, commonly known as low-voltage anode effects. This approach considers the electrolysis cell as an assembly of twenty discrete volumes with respective alumina concentration and current density. Those discrete volumes are coupled by convective-diffusive mass transfer factors. The mathematical model is composed of seven sub-models, all detailed in this paper. Five of these are designed to assess the alumina concentration of every region, for every time step. They are the feeding, the dissolution, the diffusion, the mass transport (convection), and metal production sub-models. Another sub-model calculates individual anode currents based on a simplified electrical network of the cell, while the remaining sub-models

evaluate if LVAE emissions should be observed in the cell under the current conditions.

Multiple validations were performed to evaluate the agreement of the simulator with real measurements. The results indicate that global cell voltage variations caused by an important change in the alumina concentration, or ACD, can be adequately represented by the simulator. However, variations with higher frequencies caused by bubbles or movement of the metal pad cannot be adequately represented as they were not considered in the design of the mathematical model. Variations in the alumina concentration caused by insufficient feedings are adequately represented by the simulator for all the four scenarios investigated. An increase of the range of alumina concentration will eventually lead to an augmentation of the standard deviation among individual anode currents caused by a redistribution of the current from regions with low alumina concentration to areas with higher concentration. The results indicate that the simulated standard deviation among individual anode currents is more sensitive to variations of the alumina concentration than the measured standard deviation in a real cell. This difference in sensitivity is beneficial for the simulator's ability to predict low-voltage anode effects, in which it was able to perform with great accuracy. Henceforth, the different validations performed demonstrate that the simulator can be used to represent the alumina distribution behavior reliably in an electrolysis cell for different scenarios as well as predicting LVAEs that could occur under such circumstances.

Simulations of the alumina distribution in the cell can also be used to improve the electrolysis process for multiple scenarios. Three examples were discussed in this article where the information provided by the simulator can be beneficial for the electrolysis process. The first investigation evaluated the impact of a change of ACD and the impact of different carbon heights on the uniformity of individual anode current distribution. The results indicate that a difference of approximately $\pm$ 15 pct is anticipated, with respect to the theoretical current driven by each individual anode under operational standards. The second investigation looked at the normal feeding behavior and pinpointed specific regions of the cell which are operating constantly under lower alumina concentrations. Knowing that different solutions could be used to reduce this problem, the simulator can be used to quickly identify the best scenario and then proceed with tests at the smelters hereafter. Finally, the effect of stopping a feeder for a specific amount of time was investigated in order to correctly deal with additional amounts of alumina fed to the bath during anode change or anode covering.

## ACKNOWLEDGMENTS

This work was financed by a BMP-Innovation grant from a partnership composed of "Fonds de Recherche du Québec – Nature et Technologies" (FRQNT), "National Science and Engineering Research Council of Canada" (NSERC), and Aluminerie Alouette Inc. The authors would like to thank Aluminerie Alouette Inc. for allowing them to perform in-situ experimental measurements as well as the permission to present these results. Special thanks to Guy Ladouceur, Marc Gagnon, Julie Salesse, and Michel Bergeron from Aluminerie Alouette for their collaboration in the experimental phase of this project. Additional thanks to Dr. Jerry Marks for providing the FTIR equipment used during the experimental campaigns.

## REFERENCES

1. A.T. Tabereaux: *JOM*, 1994, vol. 46 (11), pp. 30–34.
2. B.P. Leber Jr., A.T. Tabereaux, J. Marks, B. Lamb, T. Howard, R. Kantameneni, M. Gibbs, V. Bakshi, and E.J. Dolin: *Light Metals*, 1998. pp. 277–85.
3. I. Berge, R. Huglen, M. Bugge, J. Lindstrom, and T.I. Roe: *Light Metals*, 1994. pp. 389–92.
4. J. Marks: *Light Metals*, 1998. pp. 287–91.
5. D. Wong, P. Fraser, P. Lavoie, and J. Kim: *JOM*, 2015, vol. 67 (2), pp. 342–53.
6. H. Asheim, T.A. Aarhaug, A. Ferber, O.S. Kjos, and G.M. Haarberg: *7th Kyoto International Forum for Environment and Energy*, 2014, Kyoto.
7. J. Thonstad., S. Rolseth, and R. Keller: *Light Metals*, 2013. pp. 883–85.
8. D. Wong and J. Marks: *Light Metals*, 2013. pp. 865–70.
9. A.A. Zarouni, M. Reverdy, A. Zarouni, and K.G. Vankatasubramaniam: *Light Metals,* 2013. pp. 859–63.
10. W. Li, Q. Zhang, J. Yang, S. Qiu, X. Chen, J. Marks, and C. Bayliss: *Light Metals,* 2011. pp. 309–14.
11. D. Wong, A.T. Tabereaux, and P. Lavoie : *Light Metals*, 2014. pp. 529–35.
12. N.R. Dando, N. Menegazzo, L. Espinoza-Nava, N. Westendorf, and E. Batista: *Light Metals*, 2015. pp. 551–55.
13. X. Chen, W. Li, S. Qiu, Y. Zhang, and C. Bayliss: *Light Metals*, 2013. pp. 877–81.
14. H. Asheim, T.A. Aarhaug, A. Feber, O.S. Kjos, and G.M. Haarberg: *Light Metals*, 2014. pp. 535–39.
15. H. Asheim, T.A. Aarhaug, E. Sandnes, O.S. Kjos, A. Solheim, and G.M. Haarberg: *ECS Transactions*, 2015, vol. 69 (15), pp. 1–12.
16. A. Jassim, S. Ahkmetov, B.J. Welch, M. Skyllas-Kazacos, J. Bao, and Y. Yao: *Light Metals*, 2015. pp. 545–50.
17. E. Batista, N.R. Dando, N. Menegazzo, and L. Espinoza-Nava: *Light Metals*, 2016. pp. 537–40.
18. L. Dion, L.I. Kiss, S. Poncsák, and C.-L. Lagacé: *JOM*, 2016, vol. 68 (9), pp. 2472–82.
19. Y. Feng, M. Cooksey, and P. Schwarz: *Light metals*, 2011. pp. 543–48.
20. S. Zhan, M. Li, J. Zhou, J. Yang, and Y. Zhou: *Applied Thermal Engineering*, 2014, vol. 73 (1), pp. 803–16.
21. T. Hofer: PhD Thesis, 2011, École polytechnique fédérale de Lausanne: Lausanne.
22. J.T. Tessier, G.P. Tarcy, E. Batista, X. Wang, and P. Doiron: *Light Metals*, 2013. pp. 713–17.
23. E. Skybakmoen, A. Solheim, and A. Sterten: *Light Metals*, 1990. pp. 317–23.
24. X. Wang: *Light Metals*, 2009. pp. 383–88.
25. B.J. Welch and G.I. Kuschel: *JOM*, 2007, vol. 59 (5), pp. 50–4.
26. Y. Feng, M. Cooksey, and P. Schwarz: *Light metals*, 2007. pp. 339–44.
27. P. Lavoie and M. Taylor: *MOLTEN16*, 2016.
28. Y. Feng, M. Cooksey, and P. Schwarz: *9th Australasian Aluminium Smelting Conference*, 2007.
29. L. Dion, J.W. Evans, L.I. Kiss, C.-L. Lagacé, and R. Victor: *Light* Metals, 2015. pp. 723–28.

30. V. Dassylva-Raymond: PhD Thesis in engineering. 2015, Université du Québec à Chicoutimi: Chicoutimi, Qc, Canada.
31. C. Kaszás, L.I. Kiss, S. Poncsák, S. Guérard, and J.-F. Bilodeau: *Light Metals*, 2017. pp. 473–79.
32. S.-O. Tremblay, D. Marceau, D. Kocaefe, C.-L. Lagacé, M. Gagnon, G. Ladouceur, and F. Laflamme: *Light Metals*, 2016, pp. 959–64.
33. L. Wang, A.T. Tabereaux, and N.E. Richards: *Light Metals*, 1994, pp. 177–94.
34. K. Grjotheim, H. Kvande, T. Foosnaes, R. Huglen, B. Lillebuen, T. Mellerud, and T. Naterstad: *Introduction to Aluminium Electrolysis—Understanding the Hall-Heroult Process*, K. Grjotheim and H. Kvande, eds., Aluminium-Verlag, Düsseldorf, 1993, pp. 22–24.
35. P. Coursol, P. Coulombe, A. Gosselin, D. Lavoie, J.-M. Simard, J. Marks, and S. Fardeau: *JOM*, 2011, vol. 63 (8), p. 109.
36. L. Dion, L.I. Kiss, S. Poncsák, C.-L. Lagacé: *ICSOBA*, 2016. Quebec City.